ACS APPLIED MATERIALS & INTERFACES

Research Article

www.acsami.org

Enhanced Electron Extraction from Template-Free 3D Nanoparticulate Transparent Conducting Oxide (TCO) Electrodes for Dye-Sensitized Solar Cells

Zhenzhen Yang,[†] Shanmin Gao,[†] Tao Li,[‡] Fa-Qian Liu,[†] Yang Ren,[‡] and Tao Xu[†,*]

[†]Department of Chemistry and Biochemistry, Northern Illinois University, Dekalb, Illinois 60115, United States

[‡] Advanced Photon Source, Argonne National Laboratory, Argonne, Illinois 60439, United States

ABSTRACT: The semiconducting metal oxide-based photoanodes in the most efficient dye-sensitized solar cells (DSSCs) desires a low doping level to promote charge separation, which, however, limits the subsequent electron extraction in the slow diffusion regime. These conflicts are mitigated in a new photoanode design that decouples the charge separation and extraction functions. A three-dimensional highly doped fluorinated SnO_2 (FTO) nanoparticulate film serves as conductive core for low-resistance and drift-assisted charge extraction while a thin, low-doped conformal TiO_2 shell maintains a large resistance to recombination (and therefore long charge lifetime). EIS reveals that the electron transit time is reduced by orders of magnitude, whereas the recombination resistance remains in the range of traditional nanoparticle TiO_2 photoelectrodes.

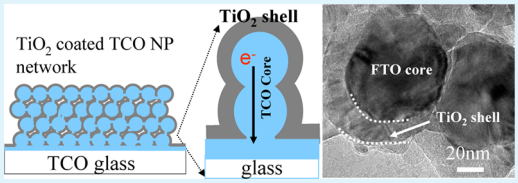

KEYWORDS: *3D TCO, 3D FTO, nanoparticles, Core-shell, conformal, DSSC*

INTRODUCTION

The quest for highly efficient photovoltaic (PV) systems often encounters conflicting demands on materials and structures. This can be particularly exemplified by, but not limited to, dye-sensitized solar cells (DSSCs) with the traditional configuration of a thick porous semiconducting layer sandwiched between a planar transparent conducting oxide (TCO) electrode and a counter electrode. The semiconducting layer typically consists of a dye-sensitized TiO_2 nanoparticle (NP) layer soaked in redox electrolyte. The sensitized TiO_2 NP layer must simultaneously capture light (through the anchored dye molecules), separate the light-induced charges, and convey the electrons to the distant TCO. The use of low doping ($<1 \times 10^{18}/cm^3$) metal oxides such as TiO_2 is to suppress the recombination at TiO_2/electrolyte interface.[1] However, such a doping level is much less than the needed redox electrolyte concentration (typically, $10^{20}/cm^3$)[2] so that electrons in TiO_2 are almost always coupled with counter ions (e.g., Li^+ from LiI).[3] Hence, electrons have to diffuse, instead of drift, in the TiO_2 NP network, because drift requires high doping level (i.e. much more free electrons than mobile counter ions) in order to build up a potential gradient in the TiO_2.[4,5] Such a diffusive transport becomes particularly problematic when a thick TiO_2 NP layer (typically over 10-μm thick) is required to anchor enough dyes for adequate light capture. This is because that a thicker TiO_2 NP film leads to more surface defect-related trapping events, and consequently, to remarkably retarded electron diffusion kinetics (typically miliseconds up to seconds across a 10 μm thick TiO_2 nanoparticle layer).[6−9] The slow diffusive transport in TiO_2 NP layer exhibits as a large transport resistance in the range of 10 to 1×10^6 Ω/cm^2 depending on voltage.[10] Therefore, introducing the more effective drift-assisted transport in photoanode would be a potential remedy to speed up electron extraction in the photoanode, which may eventually allow the use of much faster redox shuttles (relative to I^-/I_3^-) with less overpotential (relative to HOMO of dyes) for a higher attainable photovoltage.[11,12] In addition, recent work shows that even for cells that have relatively high charge-collection efficiencies, making transport faster and recombination slower can further improve the cell performance, because the dark current increases exponentially with transport resistance.[13]

However, the dilemma is that drift transport requires the use of heavily doped semiconductors, which always lead to rapid recombination at semiconductor/electrolyte interface, e.g. in SnO_2-based photoanode.[14−20] Hence, to date, most efforts in improving transport of DSSCs have focused on exploration of new architectures for existing low doping semiconducting materials (TiO_2 or ZnO, etc.) with fewer defects[21−23] and/or greater carrier mobility.[6,7,24,25]

In contrast, the drift transport in TCO electrodes (a widely used component in DSSCs and usually considered as metallic behavior[26]), has received much less attention in terms of its role in electron extraction. This is because in conventional DSSCs, a planar TCO electrode is used and placed at the very end of electron transport pathway such that the slow diffusive transport in the rather thick nanoparticulate TiO_2 layer still bottlenecks the overall charge extraction kinetics regardless the fast drift transport in the planar TCO layer.[27−29] TCO has a high conductivity over $>1 \times 10^3$ S/cm, (1×10^7 times greater

Received: June 18, 2012
Accepted: July 26, 2012
Published: July 26, 2012

than TiO_2[30]) due to its high carrier concentration (>1 × 10^{20}/cm^3) and carrier mobility(65 $cm^2 V^{-1} s^{-1}$).[31]

With all these regards, it is worth scrutinizing the functions of TCO in DSSCs for the purpose of enhancing charge extraction. In conventional DSSCs using a planar TCO, the primary role of the TCO electrode is to extract charges from the base of the TiO_2 NP layer to the external circuit (metal wires), while still allowing incident light to be transmitted.[30,32]

In this sense, a rational electron extraction scheme would be to minimize the transport distance in the slow (diffusive transport controlled) TiO_2 layer by relocating the TCO from the base of the TiO_2 NP layer into the close proximity of the TiO_2–dye interface where charge separation occurs, while still retaining sufficient surface area of the TiO_2 layer. To achieve this goal, we aim to aggressively alter the 2D flat TCO film to become an integral 3D TCO NP network with all TCO surfaces shelled by a thin conformal TiO_2 layer. Hence, not only is the large surface area of TiO_2 layer preserved for sufficient dye loading, but the TCO is simultaneously brought in the proximity of TiO_2-dye interface for rapid and drift-assisted charge extraction right after charge separation. In this way, the primary responsibilities of the conformal TiO_2 layer are streamlined to focus only on anchoring dyes and maintaining a large recombination resistance (desiring light doping) at TiO_2/electrolyte interface, whereas the contradictory demand on TiO_2 layer, namely, charge transport (desiring heavy doping), is decoupled and afforded primarily by the TCO NP core, because the light-injected electrons from the TiO_2–dye interface only need to traverse a ultrathin layer of TiO_2 prior to being extracted by the highly conductive TCO core via a drift-assisted transport.

Previously, only a handful of innovations on the structures of TCO were reported including a conformal ultrathin layer of ITO on the surface of nanoporous anodic alumina coated by atomic layer deposition (ALD) method,[33] our work on wet chemistry synthesis of inverse opal nanoporous FTO,[34] and a recent report of patterned FTO films.[35] However, all these three approaches require either the use of templates as support in the final device or during the preparation, or nanoimprinting and reactive ion etch techniques, which all limit their scalability and cost-effectiveness.

As depicted in Figure 1, to achieve this new charge extraction strategy, TCO nanoparticles are first sintered into TCO nanoparticulate network on a planar TCO substrate to serve as an integral electron-collecting anode. Next, all the surfaces of the TCO are coated with a thin and conformal layer of polycrystalline anatase TiO_2 (a few tens of nm) using atomic layer deposition (ALD) technique, followed by dye sensitization of this ALD-coated TiO_2 shell layer. The sensitized thin conformal TiO_2 layer serves as light absorber and charge separation layer, and reduces the shunt leak from TCO to electrolyte and/or to dye^+ cations. Compared to the electron diffusion distance (d_e) of >10 μm required in the conventional TiO_2 nanoparticulate photoanode, this configuration requires a d_e through the TiO_2 layer of only a few tens of nm, a factor of 1 × 10^2 to 1 × 10^3 times shorter than a 10 μm thick sensitized TiO_2 NP layer in conventional DSSCs. As diffusive transport time (τ_d) in TiO_2 is proportional to $1/d_e$,[2,26] we expect very short transport times through the nanometer thick TiO_2 layer followed by low resistive, drift-assisted extraction in the TCO NP layer to the external circuit.

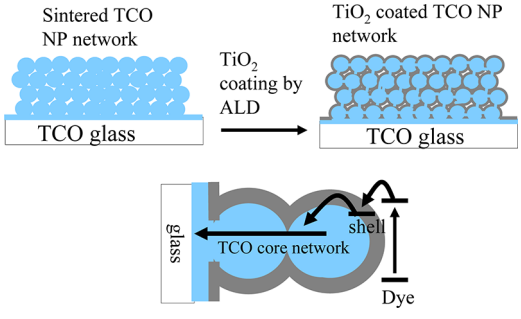

Figure 1. Schematic design for fabricating TiO_2-coated TCO network-based photoanode architecture. Note that the TCO NPs are sintered to be interconnected prior to ALD.

In this work, we chose FTO NPs rather than ITO to construct the TCO NP network. FTO is a degenerate semiconductor (metallic behavior) when highly doped (>1 × 10^{21} cm^{-3}).[36] For practical applications, FTO offers a better thermostability than ITO (the conductivity of which begins to decrease at 450 °C in flowing air or O_2,[37] used in the most efficient TiO_2 layers for DSSCs).[38] Furthermore, for mass production, FTO projects a potentially lower cost than ITO, because indium, an element with low natural abundance,[39] is the main component (>90 wt %) in ITO.[38]

EXPERIMENTAL SECTION

Fluorine-Doped SnO_2 Nanoparticle Synthesis. The procedure for preparing the F-doped SnO_2 nanoparticles is described as following. First, 1.98 g of $SnCl_2 \cdot 2H_2O$ (99.0%), 0.74 g of NH_4F, and 0.35 g of starch were completely dissolved in 30 mL of DI H_2O at 70°C. Under stirring, 25% concentrated $NH_3 \cdot H_2O$ was added dropwisely to the solution to adjust the pH of solution to 10–11. The color of solution turns to pale yellow as the $NH_3 \cdot H_2O$ increased. Next, the resulting suspension was placed in the water bath at 70°C with continuous stirring until most of the solvent was evaporated. Then the slurry was dried at 120°C in the oven overnight to remove the residue solvent. Finally, the powder was ground completely in an agate mortal and further thermally calcinated at 550 °C for 2 h. The resulting powder was pale gray. The pure SnO_2 particles were synthesized using the similar procedure without adding NH_4F.

Photoelectrode Preparation and Surface Modification. The results reported in this work were obtained with the electrodes prepared from the synthesized F-doped SnO_2 nanoparticles. In a typical sample preparation process, a slurry solution of FTO and pure SnO_2 nanoparticles were as prepared respectively by grinding a mixture of 0.1 g of FTO powder, 20 μL of acetic acid, 100 μL of DIH_2O, and 200 μL of ethanol. The particle dispersions in the mortar were transferred to a small beaker by 2 mL of ethanol and then 600 μL of ethyl cellulose (5% ethanol solution) and 0.3 g of Terpinol were added into the mixture, followed by stirring and sonication. The contents in dispersion were concentrated by evaporating at 35 °C under stirring. The pastes were finalised with a grinder. Scotch tape was used to define the area to be coated with FTO powder film. Approximately 20 $\mu L/cm^2$ paste was uniformly spread onto the entire FTO substrate. A doctor blade was used to scratch off excessive paste above the scotch tape and the FTO paste film was vertically pressed by a press to assure the uniform thickness on all sample areas. The samples were dried at room temperature for 30 min prior to sintering at 500 °C for 30 min (temperature rising rate = 1 °C/min). This process yielded an approximately 8 μm thick FTO NP (60 nm in diameter) film confirmed by scanning electron microscope.

For the surface modification of FTO nanoparticulate-based electrode, ALD method was employed to form a thin layer of dense coating as electron blocking layer on the FTO surface. ALD is the most suitable technique to produce high-quality films with excellent reproducibility and superior conformal growth on various morphologies. The FTO samples were coated with TiO_2 by ALD (Cambridge

Nanotech Savannah 200) at 200 °C using titanium tetraisoproxide (TTIP, Aldrich) at 80°C and H_2O at room temperature. The pulse/exposure/purge sequence for TTIP was 1.5 s/5 s/20 s and for H_2O was 0.015 s/5 s/20 s. The growth rate was estimated to be ~0.2 Å/cycle from ellipsometry on a witness Si chip that showed 14 nm of TiO_2. This rate is somewhat lower than those typically observed for TiO_2 ALD on flat substrates that do not required long precursor exposures (0.3 Å /cycle).

Prior to dye-loading, the photoelectrodes were heated to 80 °C, then, they were immediately soaked in a 0.3 mM solution of cis-bis(isothiocyanato) bis(2,2̂-bipyridyl-4,4̂-dicarboxylato)-ruthenium(∏) bis-tetrabutylammonium (N719) in absolute ethanol for overnight. The samples were then rinsed with ethanol for 30 min to remove non-chemisorbed dye molecules. The dye-sensitized solar cells were assembled by sandwiching the FTO NP coated with TiO_2 photoanode with the Pt-coated FTO cathode using a piece of hot melt surlyn (25 μm thick, Solaronix) as a spacer. The internal space of the cell was filled with a commercial electrolyte EL-HSE (Dyesol) by capillary force. A black mask with a window area of 0.25 cm^2 was applied on the photoanode side to define the same active area for both devices.

Photoelectrode Characterization. In a typical experiment for probing the crystalline structural of the synthesized FTO nanoparticles, the fluorine-doped SnO_2 powders and undoped SnO_2 were sealed in a small capton tube. XRD patterns were continuously collected in a high-energy (115 keV) synchrotron X-ray beam at Advanced Photon Source. The doping of Fluorine was confirmed by X-ray photoelectron spectra (XPS) measurements, which were carried out on an X-ray photoelectron spectrometer (ESCALAB MK II) using Al Kα (1486.6 eV) X-rays as the excitation source, with C 1s (284.6 eV) as the reference.

The conductivity of the synthesized FTO material was measured on the pellets of the FTO using four-probe method. Pellets (10 mm in diameter, ~0.5 mm in thickness) of the powder materials were prepared using a press (pressure = 30 MP). Current and voltage were supplied and measured by a Jandel HM21 multiheight four-point sheet resistance measurement system. The conductivity σ of the compressed pellet can be calculated by the equation: $\sigma = ((\ln 2)/(\pi t))(I/V)$, where σ is the conductivity, t is the pellet thickness, I is the applied current, and V is measured voltage, respectively.

The morphology of the photoelectrodes was observed with a scanning electron microscope (SEM, JEOL 400) and a FEI Tecnai F20ST TEM/STEM using an accelerating voltage of 200 kV.

The $J-V$ curves of the solar cells were measured by a potentiostat (Gamry Reference 600) at one Sun 1.5 AM G provided by a solar simulator (Photo Emission Inc. CA, model SS50B). The Gamry Reference 600 potentiostat was equipped with an EIS 300 software to conduct the electrochemical impedance spectroscopy (EIS) study. The EIS spectra were obtained by applying open circuit voltage as forward bias potentials in a frequency range from 0.06 to 60 kHz with an AC amplitude of 10 mV. All the EIS spectra were fitted and values were extracted by using Z-View software with an equivalent circuit (Figure 7c). Although the value of transport resistance in FTO NP-based DSSCs is small and falls in the range of fitting error, it is fitted to show the relative changes with potential.

The dye loading amount was measured by immersing the sensitized photoelectrodes into 10 mM KOH solution for 30 min to desorb and completely deprotonate the dye. The loading amount of the resulting solutions was calculated from the absorbance of solutions with respect to the calibration solutions under UV–vis spectrophotometer (Perkin Elmer, Lambda XLS+).

RESULTS AND DISCUSSION

A high energy X-ray probe is used to examine the crystal structure of the prepared FTO nanoparticles under diffraction mode. Figure 2 shows the XRD pattern of synthesized FTO nanoparticles. The major peak centered at 2θ = 1.78° is ascribed to the (110) preferential orientation. The peaks at 2.26°, 2.71° and 3.58° are associated with the (101), (200), and

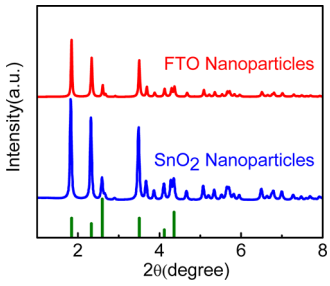

Figure 2. X-ray diffraction pattern of the synthesized FTO and pure SnO_2 nanoparticles, measured by a high-energy (115KeV, wavelength ~0.1079 Å) synchrotron X-ray beam.

(211) orientation, respectively.[40] The spectrum clearly reveals the presence of crystalline FTO with the tetragonal structure, and agrees well with the crystal phase of pure SnO_2. However, the peaks associated with dopant fluorine can not be detected by XRD even under high-energy X-ray. The presence of fluorine doping in SnO_2 was instead verified by X-ray photoelectron spectroscopy (XPS) measurements.

XPS experiments were performed to elucidate the chemical state of elements in the FTO nanoparticles. Figure 3a shows

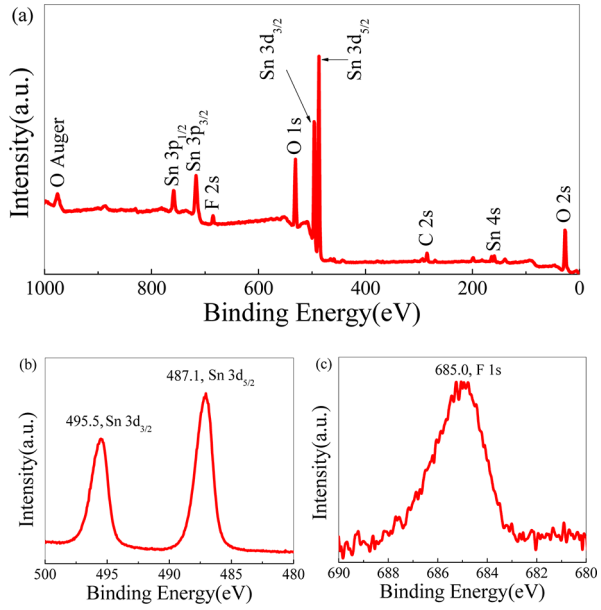

Figure 3. XPS spectra of FTO nanoparticles. (a) XPS spectra of the wide scan of FTO nanoparticles, (b) high-resolution XPS spectra for Sn 3d, (c) high-resolution XPS spectra for F 1s.

the survey XPS spectrum and panels b and c in Figure 3 are the high-resolution XPS spectrum of Sn_{3d} and F_{1s}. The survey spectrum (Figure 3a) clearly indicates that Sn, O, and F elements exist in the FTO nanoparticles, with only trace impurity of carbon, at levels that suggest adventitious hydrocarbon during sample preparation. The Sn $3d_{5/2}$ and Sn $3d_{3/2}$ spin-orbital splitting photoelectrons for FTO were located at binding energies of 487.1 and 495.5 eV (Figure 3b), respectively, typically assigned to the presence of a Sn^{4+}. This also indicates that Sn–F bonds have formed in the FTO nanoparticles.[40] Binding energy values for the F1s peaks are in the ranges 684.7–685.2 eV (Figure 3c). These values can be attributed to F^- in SnF_4.[41] This further illustrates that F ions are successfully doped into the SnO_2 lattice.

dx.doi.org/10.1021/am301090a | ACS Appl. Mater. Interfaces 2012, 4, 4419–4427

The electrical conductivity of the FTO NPs was first quantitatively studied by four-probe measurement on the pressed pellets of the nanoparticles. For comparison, pellets of undoped pure SnO_2 nanoparticles (prepared by the same method for FTO except that no NH_4F was added in the precursory solution, diameter is ~60 nm) and the anatase TiO_2 nanoparticles pellet (20 nm in diameter) were also measured. The sheet resistances were summarized in Table 1. Clearly,

Table 1. Comparison of Sheet Resistance of Pellets and Sintered Nanoparticles on FTO Substrates for FTO, Pure SnO_2 and TiO_2 NPs

	nominal sheet resistance(Ω/sq)		
sample	FTO NPs	SnO_2 NPs	TiO_2 NPs
pressed pellets	76	487	$>1 \times 10^8$
sintered NPs on a FTO substrate	9−11	87	$>1 \times 10^8$

pellets made from FTO NPs has much lower sheet resistance (~76 Ω/square) compared to that of SnO_2 (~487 Ω/square), which is conductive due to oxygen vacancies,[42] and compared to TiO_2 pellets which has a resistance beyond the upper detection limit (1×10^8 Ω/square) of our system. The calculated corresponding conductivity (see the Experimental Section) of our FTO NP is 0.27 S/cm, in agreement with the FTO powder synthesized via the sol−gel method,[42] but noticeably higher than that of SnO_2 NP pellets (0.041 S/cm).

Next, a film of FTO NP paste is applied onto a planar FTO substrate. After sintering at 500 °C, the FTO NP layer and the planar FTO film are bound together to form an integral nanoparticulate electron extraction layer. The nominal sheet resistance of these sintered FTO nanoparticulate film on a planar FTO glass consistently falls in the range of 9−11 Ω/square. This value consists of the cross-film resistance (in vertical direction) of the FTO NP film and the lateral resistance of the underneath planar and compact FTO film. Note that drift-transport always goes though this least-resistive path in an electrical circuit. In contrast, SnO_2 NP film on FTO shows a higher value of 87 Ω/square, whereas the resistance of TiO_2 NP film on FTO is too high to be measured.

Then, a conformal shell of TiO_2 is deposited over all surfaces of the FTO nanoparticulate film as well as the FTO substrate. This thin TiO_2 layer reduces the electron back transfer from FTO (both nanoparticles and the continuous underneath FTO film) to electrolyte (shunt leakage) in DSSCs.[34,43] Ideally, this layer should be pinhole-free and covers all surfaces of FTO NP layer. For this purpose, we utilize ALD technique, which is a layer-by-layer deposition technique that has previous been used to achieve conformal films on various morphologies.[44−46]

In Figure 4, the depth profile of the ALD TiO_2 shell layer was studied by scanning transmission electron microscopy (STEM) coupled with energy-dispersive X-ray (EDX). Figure 4a shows the result from STEM investigation of the photoelectrodes. Figure 4b is the magnified image of the portion of the connected FTO nanoparticles. The core-shell structure is clearly presented. The average particle size of the synthesized FTO is around 60 nm, and the ALD TiO_2 layer is compact and uniform with thickness around 20−25 nm. The organic fillers e.g. ethyl cellulose in the FTO paste decompose upon sintering, which leaves space for coating the conformal TiO_2 layer by ALD method. Figure 4c shows the dark-field image of a typical TCO (core)−TiO_2 (shell) conformal nanoparticulate photoanodes, in which the FTO core particles are sintered together,

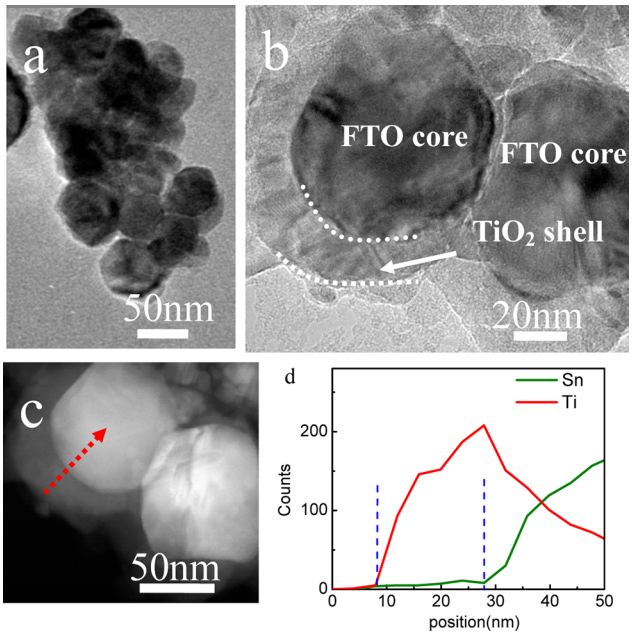

Figure 4. Typical STEM images of the synthesized FTO nanoparticle coated with 20 nm TiO_2 by ALD method. (a) Low-magnification image; (b) close investigation showing the size of the particle and the coating of TiO_2. (c) HAADF-STEM image of the connected FTO particles and the corresponding (d) EDX and line scan profile confirm the Ti residing predominantly in the shell and Sn in the core. All films were first sintered to 500 °C prior to surface treatment. To aid the reader, some regions of the TiO_2 shells are indicated.

and wrapped by the TiO_2 shell. In Figure 4d, the corresponding profile of EDX line scans were acquired across the FTO-(core)−TiO_2(shell) structures indicated by the arrow in Fig. 4c. For a core-shell structure, the EDX signal of the shell material is expected to be proportional to the thickness of the shell in the z direction (i.e., normal to the plane of incidence).[47] Therefore, the intensities of the Ti, and Sn signal change with the probe position across the measured portion. As the electron beam scans from the edge to the center, only Ti signal is detected and grows because the e-beam impacts more Ti when it scans from edge to center, whereas no Sn signal is observed in the portion near the edge region (approximately ~20 nm). As the electron-beam approaches the center, Sn signals start to grow. The TEM study clearly confirms the formation of the desired TCO(core)-TiO_2(shell) nanoparticulate structure. However, we also observed small amount of pinholes presented in the TEM, which may result from the further firing of the ALD TiO_2 layer after ALD deposition. Thus, minimizing the pinholes in the ALD TiO_2 layer is certain a focus for future improvement.

The photovoltage and photocurrent of DSSCs based on the conformal TCO(core)−TiO_2(shell) NP film (8 μm thick, with dye-loading of 7.1×10^{-8} mol/cm^2, approximately 30% of the best TiO_2 NP-based DSSCs[1]) were characterized under the simulated AM 1.5 illumination(100mW/cm^2). For comparison, DSSCs based on 8-μm-thick NP films using unshelled FTO NPs, and undoped SnO_2 NPs with/without TiO_2 shell layer were also measured. Typical $J-V$ curves of these DSSCs are shown in Figure 5. The photovoltaic parameters from the $J-V$ measurement are summarized in Table 2, including open circuit voltage (V_{oc}), short-circuit current (J_{sc}), energy conversion coefficient (η), and fill factor (FF).

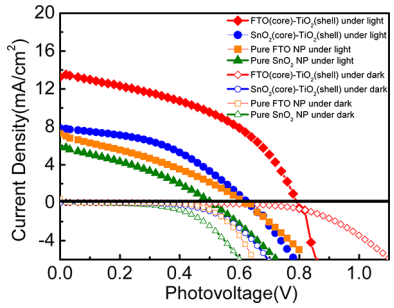

Figure 5. Typical $J-V$ curves of DSSCs based on FTO NPs (with and without TiO_2 shell), and undoped SnO_2 NPs (with and without TiO_2 shell) under AM 1.5 G illumination and under dark, respectively. The area of both devices is 0.25 cm^2.

Table 2. Averaged Photovoltaic Parameters of DSSCs Based on Five Pairs of Samples, Including FTO NP-Based DSSCs (with and without TiO_2 shell), and Undoped SnO_2 NP-Based DSSCs (with and without TiO_2 shell) with Same Thickness and Dye Loading Amount

	J_{sc} (mA/cm^2)	V_{oc} (mV)	FF	η (%)
FTO(core)-TiO_2(shell)-	13.0 ± 0.30	760 ± 20	0.48 ± 0.02	4.6 ± 0.2
unshelled FTO NP-based DSSC	8.0 ± 0.30	600 ± 20	0.30 ± 0.02	1.5 ± 0.2
undoped SnO_2(core)-TiO_2(shell)	7.6 ± 0.20	600 ± 20	0.45 ± 0.03	2.1 ± 0.2
unshelled SnO_2NP-based DSSC	5.6 ± 0.20	480 ± 20	0.33 ± 0.02	1.0 ± 0.2

It is clear that the samples using conformal FTO(core)−TiO_2(shell) NP photoelectrodes exhibit the highest current density by a factor of 1.6 in J_{sc} relative to the DSSCs based on undoped SnO_2 NPs with TiO_2 shell. This is because the lower series resistance in FTO NP network than in SnO_2 NP network and the reduced shunt leak by the presence of TiO_2 shell layer than its absence. Furthermore, as summarized in Table 2, the V_{oc} of DSSCs based on the conformal FTO(core)−TiO_2(shell) NP photoanodes were measured to be consistently ~770 mV, nearly 150 mV greater than the value for DSSCs based on undoped SnO_2 NPs shelled with TiO_2, 150 mV greater than unshelled FTO, and 350 mV greater than unshelled SnO_2. As a reference, the literature reported V_{oc} values for bare SnO_2 NP-based DSSCs are also below 600 mV.[15,17,18,48]

It is obvious that TiO_2-shelled nanoparticles of FTO and SnO_2 all exhibit much higher V_{oc} and less dark currents than their respective unshelled counterparts. First of all, this confirms that the use of relatively light doping active layer as shell can reduces the recombination at active layer−electrolyte interface (shunt leak). Thus, the fill factors of TiO_2 shelled NPs are also better than unshelled NPs. We noticed the relatively low fill factor of our cells. This could be the defective sites (e.g., pinholes) in the ALD-TiO_2 shell layer that is not adequately compact to seamlessly shell the FTO core, and this certainly needs to be improved in our future work. Second, LUMO of dye molecules has a less overpotential relative to the conduction band edge of TiO_2 (−4.2 eV vs Vac)[49] than to FTO (approximately −4.8 eV vs Vac.)[49,50] or SnO_2, leading to higher attainable photovoltages of the TiO_2 shelled NPS than unshelled NPs.

The FTO NPs have a greater V_{oc} than SnO_2 NPs, either shelled with TiO_2 or unshelled. In principle, V_{oc} is determined by the energy gap between the quasi Fermi level of the photoanode under illumination and the redox potential of the I^-/I_3^-.[51] With heavy doping of F, the Fermi level of FTO rises due to Burstein−Moss shift,[52] and the high density of states (DOS) in FTO[53] (~6 times greater than that in pure SnO_2) makes it nearly metallic behavior[30,36,54] to accommodate more electrons than undoped SnO_2. Consequently, the quasi-Fermi level of FTO can be charged all the way to the conduction band edge of the TiO_2 shell (Figure 6). In contrast, undoped SnO_2

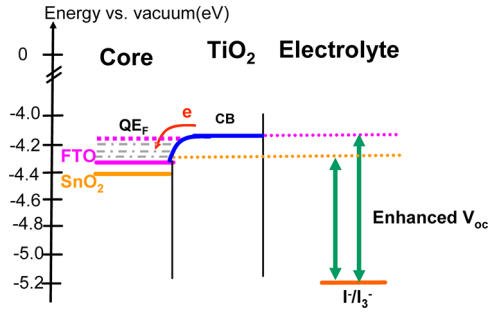

Figure 6. Scheme of energy diagram at the interface between FTO/or pure SnO_2 and TiO_2 in contact with electrolyte based on I^-/I_3^-.

has fairly scattered and low DOS near the CB edge of TiO_2,[53,55] so that fewer electrons can be accommodated near the CB edge of TiO_2 in SnO_2, leading to its low V_{oc}.

In principle, the FTO−TiO_2 interface can be treated as a metalln-type junction. To counter-balance the Fermi level difference in FTO (e.g., FTO, approximately −4.8 eV vs vac.)[49,50] and TiO_2 (approximately −4.4 eV vs vac.),[49] electrons have to flow from TiO_2 to TCO layer at the TCO/TiO_2 interfaces, resulting in an electron-depletion layer (space charge layer) in TiO_2 with a built-in potential of 0.4 eV (difference in Fermi levels between TiO_2 and FTO), i.e., band bending.[56,57] Under illumination, the electrons are injected to the TiO_2. Then, the conduction band of TiO_2 inclines to FTO, and the electrons can favorably drift downhill from TiO_2 to FTO.[28,58,59] However, this tiny portion of drift transport is negligible in the conventional photoanodes consisting of a very thick layer of TiO_2 or ZnO-based nanostructures (nanoparticles or nanowires) on a flat TCO substrate, because the width of the depletion layer spans only ~30 nm in the TiO_2 layer adjacent to the TCO substrate.[60] As such, majority transport in the rest of the thick TiO_2 layers is not affected. In contrast, in our FTO (core)−TiO_2 (shell) conformal NP photoanodes, the TCO/TiO_2 interfaces are omnipresent so that this space charge layer in TiO_2 shell should not be omitted.

Ideally, such FTO/TiO_2 interface would be an Ohmic contact for best performance. However, we noticed that the FTO/TiO_2 interface in our FTO (core)−TiO_2 (shell) conformal NP photoanodes appears more or less a Schottky contact. This can be indirectly seen by the suppressed onset of the dark current (see Figure 5), because dark current (i.e. electrons flow from FTO to TiO_2 under dark) is analog to a metalln-type Schottky junction at reverse bias (electrons flow from metal to n-type semiconductor), which further increases the barrier height, resulting in the further suppressed dark current (under dark).

We then investigated the time constants of the two kinds of the DSSCs using EIS technique, which is an effective way to

elucidate the competition between the electron lifetime and the electron diffusion kinetics to the collecting TCO anode. Figure 7a compares the Nyquist plot of an updoped SnO_2 NP film

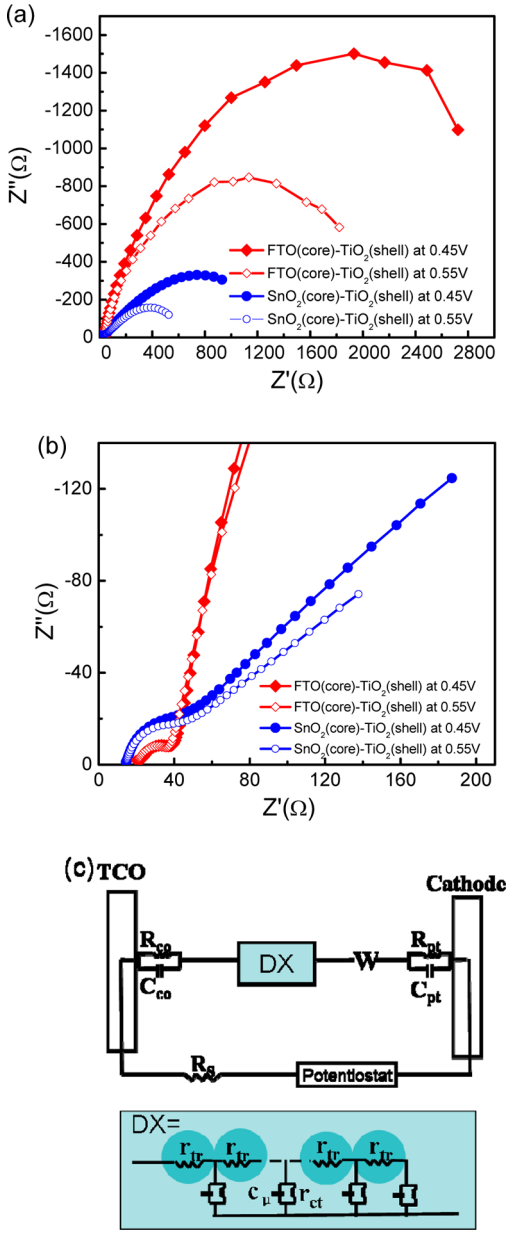

Figure 7. (a) Nyquist plots of representative EIS data at 450 and 550 mV forward bias in the dark condition for FTO-based DSSC (red circle) and SnO_2-based DSSC (blue triangle) and (b) their magnified part at high frequency. (c) the equivalent circuit used for fitting data from EIS measurement.

with that of a conformal FTO(core)−TiO_2(shell) nanoparticulate DSSC. The impedance data were measured at a forward bias of 0.45 and 0.55 V in the dark at 20 °C in the presence of I^-/I_3^- redox electrolyte. An enlarged diameter of the semicircle was observed in the low frequency range (right) from FTO NP-DSSC compared to that of the undoped SnO_2 NP film. Because this diameter corresponds to the resistance of heterogeneous charge transfer (R_{ct}) from the conduction band of the semiconductor to tridiodide ions in the electrolyte, the increase indicates that the FTO(core)−TiO_2(shell) leads to a pronounced reduction in the dark current. The very small semicircle magnified in Figure 7b at high frequency is assigned to the resistance of Pt and capacitance C_{pt} of the electrolyte|Pt cathode interface. All the EIS spectra were fitted by using Z-View software with an equivalent circuit (Figure 7c), which is based on the general transmission line model.

To investigate the origin of the high V_{oc} obtained for FTO cell, we plot the fitted parameters (R_{tr}, R_{ct}, C_μ) as a function of the Fermi level (V_F) in the sensitized photoanode for the cells. V_F, the internal voltage, is obtained by subtracting the effect of the series resistance and counter electrode charge transfer resistance on both R_{tr} and C_μ as follows: $V_F = V_{app} - V - V_{CE}$, where V_s and V_{CE} are the potential drop at the series resistance and at the counter electrode, respectively.[49,61] Figure 8a plots the transport resistance (R_{tr}) of the cells analyzed and Figure 8b plots the chemical capacitance against V_F, respectively.

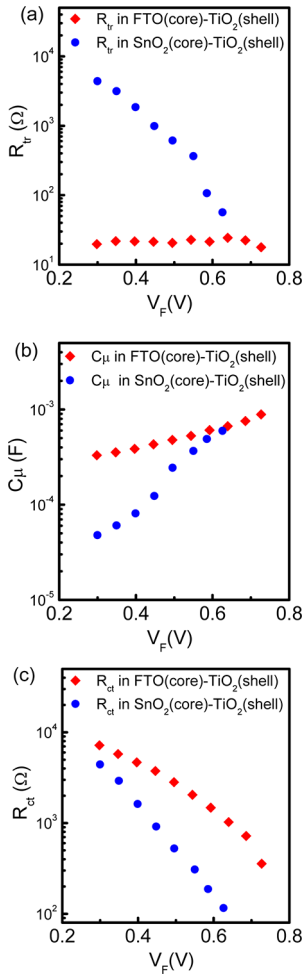

Figure 8. Characteristic cell data with a dependence on the internal voltage extracted from the EIS spectra: (a) electron transport resistance R_{tr}, (b) chemical capacitance $C\mu$, (c) interfacial charge recombination resistance R_{ct}.

For pure SnO_2 cell, we see that the resistances R_{tr}, R_{ct}, and the capacitance (C_μ) of the film changes with bias as in the case of conventional TiO_2 NP-based photoanode.[10] In particular, an exponential decrease of the R_{tr} is observed as the voltage increases. A nearly constant value of the capacitance is obtained at low potentials, followed by an exponential increase because electron accumulation in the Fermi level of SnO_2 increases with the potential.

However, in our FTO(core)-TiO_2(shell) conformal nanoparticulate photoanode, the R_{tr} are $10-10^3$ times (depending on voltage) lower than that of the undoped SnO_2 NP-based photoanodes. Moreover, R_{tr} of our FTO(core)−TiO_2(shell) photoanode exhibits much less dependence on bias in comparison to the SnO_2 NP-based photoanodes, as well as conventional TiO_2 NP-based photoanodes.[10] We suggest that this is because the TiO_2 layer is extremely thin and that electrons only need to transport across the thickness of the TiO_2 layer. The transport time associated with TiO_2 layer is significantly reduced compared to transport in the conventional DSSCs. Thus, the rate-determining step for transport is likely associated with electron transport across the 3D-FTO network, which is highly metallic. Therefore, weak dependence of transport resistance on bias voltage is observed. This agrees with the conductivity measurement summarized in Table 1.

Furthermore, in Figure 8b, the value of capacitance in our conformal FTO(core)−TiO_2(shell) nanoparticulate photoanode is nearly 10 times greater than that of SnO_2 NP-based photoanode. If the capacitance C_μ is taken to be strictly "chemical" in nature, it should reflect the density of states (DOS) in both FTO NPs and TiO_2 shell. Fluorine doping increases the DOS in SnO_2. This agrees with the recently report on the doping effect on capacitance, which obeys Mott−Schottky characteristics in highly doped case.[62] Furthermore, the chemical capacitance of the conformal FTO(core)−TiO_2(shell) nanoparticulate photoanode also varies relatively slowly with bias, in comparison to undoped SnO_2 NP-based photoanodes, as well as to conventional TiO_2 NP-based photoanodes.[10] In TiO_2 nanoparticulate photoanodes, the incoming photoelectrons can readily fill the DOS in TiO_2, which results in its nearly exponential rise of capacity upon the increase of voltage.[62,63] In contrast, because of the high DOS in FTO in our FTO(core)−TiO_2(shell) NP photoanodes, it requires more photoelectrons to reach the similar level Fermi level. Furthermore, we think the built-in potential at FTO/TiO_2 interface may induce drift transport in TiO_2 layer, and may also increase the Helmholtz capacitance at TiO_2/electrolyte interface because the thickness of TiO_2 shell (25 nm) is comparable to the thickness of space charge layer (~30 nm)[27,28] at the FTO/TiO_2 interface. For drift transport, the number of charges per unit volume is limited only by the photocarrier generation rate and the intrinsic carrier mobility in FTO,[31] whereas in diffusive transport, the capacitance is limited by the available DOS and the Helmholtz capacitance at the TiO_2/electrolyte interface.

Figure 8c shows the interfacial charge recombination resistance (R_{ct}) of the FTO(core)−TiO_2(shell) NP photoanodes and the undoped SnO_2 (core)−TiO_2 (shell) photoanodes. The FTO(core)−TiO_2(shell) NP photoanodes shows voltage-dependent R_{ct} within 1×10^2 to 1×10^4 Ω. This value is not as good as the best TiO_2 NP-based photoanodes (10 to 1×10^6 Ω) because of imperfect covering of the ALD TiO_2 layer. For example, at 0.6 V, R_{ct} is around 1×10^3 Ω for the FTO(core)−TiO_2(shell) NP photoanodes, whereas it is 1×10^5 Ω for TiO_2 NP-based photoanode,[63] but it is still comparable considering the fact that the TiO_2 shell is only 20−25 nm thick and the conventional TiO_2 NP-based electrode is a solid TiO_2 layer. Moreover, in comparison to the cells based on SnO_2(core)−TiO_2(shell) photoaondes, the R_{ct} FTO(core)−TiO_2(shell) NP photoanodes is less voltage dependent and relatively remain at high values. This could be caused by the Schottky barrier at FTO−TiO_2 interface, over which the back electron transfer has to overcome.

If we assume a multiple trapping diffusion interpretation, the charge lifetime is calculated by $\tau_n = R_{ct}C_\mu$.[7,64] Figure 9a is the

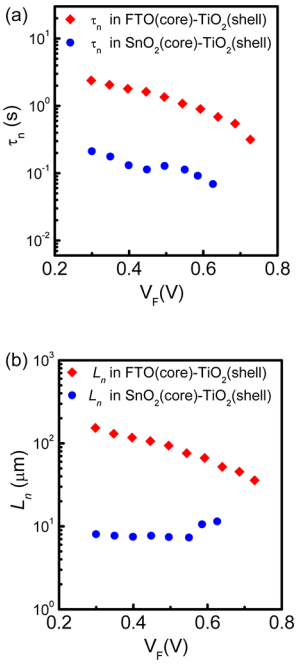

Figure 9. (a) Calculated electron life time, (b) calculated ffective diffusion length L_n in FTO(core)−TiO_2(shell) DSSC compared to a conventional nanoparticle SnO_2 DSSC.

comparison in charge lifetime (τ_n) for the FTO(core)−TiO_2 (shell) based DSSC and pure SnO_2 DSSC. τ_n decreases exponentially with the increase of the applied voltage for all the cells. Because of an increase in R_{ct} and C_μ with doping and TiO_2 coating, the electron lifetime for the FTO(core)-TiO_2 (shell) photoanode DSSC exceeds that of pure SnO_2 cell at all applied voltages. The longer electron lifetime in the FTO(core)−TiO_2 (shell) cell shows the remarkable suppression of the charge recombination at the oxide/dye/electrolyte interface, because electrons only traverse 20 nm in TiO_2 layer prior to being dragged to the FTO core by the built-in potential at FTO/TiO_2 interface. Furthermore, the faster electron transport in FTO core outpaces the recombination at TiO_2/electrolyte interface. Hence, more electrons can reach the external circuit, which results in an enhanced J_{sc} in our device as indicated in Table 1.

The competition between the collection and the recombination of electrons can be expressed in terms of the electron diffusion length (L_n), according to equation: $L_n = ((R_{ct})/(R_{tr}))^{1/2}$.[10] An electron diffusion length much greater than the photoanode film thickness ascertains effective collection of photo-generated charge carriers.[65,66] As shown in Figure 9b, the calculated electron diffusion length values, 35−140μm depending on the potential, are significantly higher than the thickness of FTO(core)−TiO_2 (shell) photoanode (~8 μm), indicating that the electron transport is not the bottleneck of our FTO(core)−TiO_2 (shell) photoanodes. Moreover, the L_n in our structure is even better than that in an efficient SnO_2 NP film. The core−shell structure is quite favorable for electron diffusion because of the TiO_2 shell layer is only 20 nm. The significant higher carrier mobility in FTO (65 $cm^2\ V^{-1}\ s^{-1}$)[31] than in TiO_2 (1×10^{-6} $cm^2\ V^{-1}\ s^{-1}$)[67] effectively redistributes

dx.doi.org/10.1021/am301090a | ACS Appl. Mater. Interfaces 2012, 4, 4419−4427

transport requirements from TiO_2 to FTO, and significantly reduces the transport time.

CONCLUSIONS

We have successfully synthesized FTO nanoparticles by template-free wet chemistry method and prepared 3D FTO-(core)-TiO_2(shell) conformal nanoparticulate photoanodes. Enhanced electron extraction assisted by drift transport mechanism was observed in photoanodes based on FTO (core)−TiO_2 (shell) conformal nanoparticle network. In comparison to undoped SnO_2 NP-based photoanodes (either shelled with TiO_2 or unshelled), the FTO(core)−TiO_2 (shell) conformal NP photoanodes exhibit enhanced J_{sc} due to less serious resistance, and increased V_{oc} due to high doping level in FTO nanoparticles with a TiO_2 shell as recombination resistor. In EIS study, the FTO(core)−TiO_2 (shell) conformal nanoparticulate photoanodes exhibit lower electron transport resistance R_{tr} and longer effective electron diffusion length than undoped SnO_2-based photoanodes, which is facilitated by the built-in voltage at FTO/TiO_2 interface and the high conductivity of FTO nanoparticle network. This work paves a way for rapid extraction of electrons in photoanodes that allows the use of faster redox with smaller overpotential for a higher attainable photovoltage than the current state-of-the-art.

AUTHOR INFORMATION

Corresponding Author

*Corresponding author, Email: txu@niu.edu.

Notes

The authors declare no competing financial interest.

ACKNOWLEDGMENTS

We acknowledge the support from National Science Foundation (CBET-1150617) and NIU-Argonne Nanoscience Fellowship via InSET. The electron microscopy was conducted at the Electron Microscopy Center for Materials Research at Argonne National Laboratory, a U.S. Department of Energy Office of Science Laboratory operated under Contract DE-AC02-06CH11357 by UChicago Argonne, LLC. The use of the Advanced Photon Source was supported by the U.S. Department of Energy, Office of Science, and Office of Basic Energy Science under Contract DE-AC02-06CH11357. We thank Dr. Alex B. F. Martinson at Materials Science Division, Argonne National Laboratory for his help with atomic layer deposition and insightful discussion.

REFERENCES

(1) Grätzel, M. *Inorg. Chem.* **2005**, *44*, 6841.
(2) Junghänel, M.; Tributsch, H. *J. Phys. Chem. B* **2005**, *109*, 22876.
(3) Kopidakis, N.; Park, E. A. S.-G.; van de Lagemaat, J.; Frank, A. J. *J. Phys. Chem. B* **2000**, *104*, 3930.
(4) Gregg, B. A.; Hanna, M. C. *J. Appl. Phys.* **2003**, *93*, 3605.
(5) Fu, D.; Zou, J.; Wang, K.; Zhang, R.; Yu, D.; Wu, J. *Nano Lett.* **2011**, *11*, 3809.
(6) Hagfeldt, A.; Boschloo, G.; Sun, L.; Kloo, L.; Pettersson, H. *Chem. Rev.* **2010**, *110*, 6595.
(7) Martinson, A. B. F.; Goes, M. S.; Fabregat-Santiago, F.; Bisquert, J.; Pellin, M. J.; Hupp, J. T. *J. Phys. Chem. A* **2009**, *113*, 4015.
(8) Cameron, P. J.; Peter, L. M. *J. Phys. Chem. B* **2005**, *109*, 7392.
(9) Peter, L. *Acc. Chem. Res.* **2009**, *42*, 1839.
(10) Wang, Q.; Ito, S.; Grätzel, M.; Fabregat-Santiago, F.; Mora-Seró, I.; Bisquert, J.; Bessho, T.; Imai, H. *J. Phys. Chem. B* **2006**, *110*, 25210.
(11) Hamann, T. W.; Jensen, R. A.; Martinson, A. B. F.; van Ryswyk, H.; Hupp, J. T. *Energy Environ. Sci.* **2008**, *1*, 66.
(12) Spokoyny, A. M.; Li, T. C.; Farha, O. K.; Machan, C. W.; She, C.; Stern, C. L.; Marks, T. J.; Hupp, J. T.; Mirkin, C. A. *Angew. Chem., Int. Ed.* **2010**, *49*, 5339.
(13) Zhu, K.; Jang, S.-R.; Frank, A. J. *J. Phys. Chem. Lett.* **2011**, *2*, 1070.
(14) Niinobe, D.; Makari, Y.; Kitamura, T.; Wada, Y.; Yanagida, S. *J. Phys. Chem. B* **2005**, *109*, 17892.
(15) Chappel, S.; Chen, S.-G.; Zaban, A. *Langmuir* **2002**, *18*, 3336.
(16) Onwona-Agyeman, B. K., S.; Kumara, A.; Okuya, M.; Murakami, K.; Konno, A. T., K. *Jpn. J. Appl. Phys. Part 2* **2005**, *44*, 3.
(17) Prasittichai, C.; Hupp, J. T. *J. Phys. Chem. Lett.* **2010**, *1*, 1611.
(18) Ramasamy, E.; Lee, J. *J. Phys. Chem. C* **2010**, *114*, 22032.
(19) Fungo, F.; Otero, L.; Durantini, E. N.; Silber, J. J.; Sereno, L. E. *J. Phys. Chem. B* **2000**, *104*, 7644.
(20) Fessenden, R. W.; Kamat, P. V. *J. Phys. Chem.* **1995**, *99*, 12902.
(21) Martinson, A. B. F.; Elam, J. W.; Hupp, J. T.; Pellin, M. J. *Nano Lett.* **2007**, *7*, 2183.
(22) Law, M.; Greene, L. E.; Johnson, J. C.; Saykally, R.; Yang, P. D. *Nat. Mater.* **2005**, *4*, 455.
(23) O'Regan, B. C.; Durrant, J. R.; Sommeling, P. M.; Bakker, N. J. *J. Phys. Chem. C* **2007**, *111*, 14001.
(24) Hochbaum, A. I.; Yang, P. *Chem. Rev.* **2010**, *110*, 527.
(25) Kang, S. H. C., S. H.; Kang, M. S.; Kim, J. Y.; Kim, H. S.; Hyeon, T.; Sung, Y. E. . *Adv. Mater.* **2008**, *20*, 54.
(26) Peter, L. M. *Phys. Chem. Chem. Phys* **2007**, *9*, 2630.
(27) van de Lagemaat, J.; Park, N.-G.; Frank, A. J. *J. Phys. Chem. B* **2000**, *104*, 2044.
(28) Rühle, S.; Dittrich, T. *J. Phys. Chem. B* **2005**, *109*, 9522.
(29) Juan Bisquert, J.; Garcia-Belmonte, G.; Fabregat-Santiago, F. *J Solid State Electrochem.* **1999**, *3*, 337.
(30) Wu, H. H., L.; Carney, T.; Ruan, Z.; Kong, D.; Yu, Z.; Yao, Y.; Cha, J. J.; Zhu, J.; Fan, S.; Cui, Y. *J. Am. Chem. Soc.* **2011**, *133*, 27.
(31) Calnan, S. T., A. N. *Thin Solid Films* **2010**, *518*, 1839.
(32) Wang, Y.; Brezesinski, T.; Antonietti, M.; Smarsly, B. *ACS Nano* **2009**, *3*, 1373.
(33) Martinson, A. B. F.; Elam, J. W.; Liu, J.; Pellin, M. J.; Marks, T. J.; Hupp, J. T. *Nano Lett.* **2008**, *8*, 2862.
(34) Yang, Z.; Gao, S.; Li, W.; Vlasko-Vlasov, V.; Welp, U.; Kwok, W.-K.; Xu, T. *ACS Appl. Mater. Interfaces* **2011**, *3*, 1101.
(35) Wang, F.; Subbaiyan, N. K.; Wang, Q.; Rochford, C.; Xu, G.; Lu, R.; Elliot, A.; D'Souza, F.; Hui, R.; Wu, J. *ACS Appl. Mater. Interfaces* **2012**, *4*, 1565.
(36) Turrión, M.; Macht, B.; Tributsch, H.; Salvador, P. *J. Phys. Chem. B* **2001**, *105*, 9732.
(37) Lee, J.-H. *J. Electroceram.* **2009**, *23*, 554.
(38) Kawashima, T.; Ezure, T.; Okada, K.; Matsui, H.; Goto, K.; Tanabe, N. *J. Photochem. Photobiol., A* **2004**, *164*, 199.
(39) Dutch, S. I. *J. Chem. Educ.* **1999**, *76*, 356.
(40) Zhi, X.; Zhao, G.; Zhu, T.; Li, Y. *Surf. Interface Anal.* **2008**, *40*, 67.
(41) Kumar, V.; Govind, A.; Nagarajan, R. *Inorg. Chem.* **2011**, *50*, 5637.
(42) Avadhut, Y. S.; Weber, J.; Hammarberg, E.; Feldmann, C.; Schellenberg, I.; Pöttgen, R.; Schmedt auf der Günne, J. *Chem. Mater.* **2011**, *23*, 1526.
(43) Yang, Z.; Xu, T.; Gao, S.; Welp, U.; Kwok, W.-K. *J. Phys. Chem. C* **2010**, *114*, 19151.
(44) George, S. M. *Chem. Rev.* **2010**, *110*, 111.
(45) Liu, Y.; Gibbs, M.; Perkins, C. L.; Tolentino, J.; Zarghami, M. H.; Bustamante, J.; Law, M. *Nano Lett.* **2011**, *11*, 5349.
(46) Sarkar, S. K.; Kim, J. Y.; Goldstein, D. N.; Neale, N. R.; Zhu, K.; Elliott, C. M.; Frank, A. J.; George, S. M. *J. Phys. Chem. C* **2010**, *114*, 8032.
(47) Abel, K. A.; Boyer, J.-C.; Andrei, C. M.; van Veggel, F. C. J. M. *J. Phys. Chem. Lett.* **2011**, *2*, 185.
(48) Tiwana, P.; Docampo, P.; Johnston, M. B.; Snaith, H. J.; Herz, L. M. *ACS Nano* **2011**, *5*, 5158.
(49) Dou, X.; Sabba, D.; Mathews, N.; Wong, L. H.; Lam, Y. M.; Mhaisalkar, S. *Chem. Mater.* **2011**, *23*, 3938.

(50) Gubbala, S.; Chakrapani, V.; Kumar, V.; Sunkara, M. K. *Adv. Funct. Mater.* **2008**, *18*, 2411.
(51) Peter, L. M. *J. Phys. Chem. C* **2007**, *111*, 6601.
(52) Klein, A.; Körber, C.; Wachau, A.; Säuberlich, F.; Gassenbauer, Y.; Harvey, S. P.; Proffit, D. E.; Mason, T. O. *Materials* **2010**, *3*, 4892.
(53) Xu, J.; Huang, S.; Wang, Z. *Solid State Comm.* **2009**, *149*, 527.
(54) Wu, H.; Hu, L.; Carney, T.; Ruan, Z.; Kong, D.; Yu, Z.; Yao, Y.; Cha, J. J.; Zhu, J.; Fan, S.; Cui, Y. *J. Am. Chem. Soc.* **2011**, *133*, 27.
(55) Munnix, S.; Schmeits, M. *Phys. Rev. B* **1986**, *33*, 4136.
(56) Jacobsen, V.; Dürr, M.; Wendling, B.; Yasuda, A.; Nelles, G.; Knoll, W.; Kreiter, M. *Appl. Surf. Sci.* **2006**, *252*, 3903.
(57) Breeze, A. J.; Schlesinger, Z.; Carter, S. A.; Brock, P. J. *Phys. Rev. B* **2001**, *64*, 125205.
(58) Rühle, S.; Cahen, D. *J. Phys. Chem. B* **2004**, *108*, 17946.
(59) Schlichthörl, G.; Park, N. G.; Frank, A. J. *J. Phys. Chem. B* **1999**, *103*, 782.
(60) Turrión, M.; Bisquert, J.; Salvador, P. *J. Phys. Chem. B* **2003**, *107*, 9397.
(61) González-Pedro, V.; Xu, X.; Mora-Seró, I. n.; Bisquert, J. *ACS Nano* **2010**, *4*, 5783.
(62) Fabregat-Santiago, F.; Garcia-Belmonte, G.; Mora-Seró, I.; Bisquert, J. *Phys. Chem. Chem. Phys.* **2011**, *13*, 35.
(63) Wang, Q.; Ito, S.; Gratzel, M.; Fabregat-Santiago, F.; Mora-Sero, I.; Bisquert, J.; Bessho, T.; Imai, H. *J. Phys. Chem. B* **2006**, *110*, 25210.
(64) Yang, Z.; Xu, T.; Y., I.; Welp, U.; Kwok, W. K. *J. Phys. Chem. C* **2009**, *113*, 20521.
(65) Wang, M.; Chen, P.; Humphry-Baker, R.; Zakeeruddin, S. M.; Grätzel, M. *ChemPhysChem* **2009**, *10*, 290.
(66) Frank, A. J.; Kopidakis, N.; van de Lagemaat, J. *Coord. Chem. Rev.* **2004**, *248*, 1165.
(67) Richter, C.; Schmuttenmaer, C. A. *Nat. Nanotechnol.* **2010**, *5*, 769.